

Inferring Flare Loop Parameters with Measurements of Standing Sausage Modes

Ming-Zhe Guo^{1,2} · Shao-Xia Chen¹ · Bo Li¹ ·
Li-Dong Xia¹ · Hui Yu¹

Received: 3 October 2015 / Accepted: 15 February 2016 / Published online: 7 March 2016
© Springer Science+Business Media Dordrecht 2016

Abstract Standing fast sausage modes in flare loops were suggested to account for a considerable number of quasi-periodic pulsations (QPPs) in the light curves of solar flares. This study continues our investigation into the possibility of inverting the measured periods P and damping times τ of sausage modes to deduce the transverse Alfvén time R/v_{Ai} , density contrast ρ_i/ρ_e , and the steepness of the density distribution transverse to flare loops. A generic dispersion relation governing linear sausage modes is derived for pressureless cylinders where density inhomogeneity of arbitrary form takes place within the cylinder. We show that in general the inversion problem is under-determined for QPP events where only a single sausage mode exists, whether the measurements are spatially resolved or unresolved. While R/v_{Ai} can be inferred to some extent, the range of possible steepness parameters may be too broad to be useful. However, for spatially resolved measurements where an additional mode is present, it is possible to deduce self-consistently ρ_i/ρ_e , the profile steepness, and the internal Alfvén speed v_{Ai} . We show that at least for a recent QPP event that involves a fundamental kink mode in addition to a sausage one, flare loop parameters are well constrained even if the specific form of the transverse density distribution remains unknown. We conclude that spatially resolved, multi-mode QPP measurements need to be pursued to infer flare loop parameters.

Keywords Coronal seismology · Magnetic fields, corona · Waves, magnetohydrodynamic

1. Introduction

There is now ample evidence for the existence of low-frequency waves and oscillations in the structured solar atmosphere (for recent reviews, see *e.g.*, Nakariakov and Verwichte,

✉ B. Li
bbl@sdu.edu.cn

¹ Shandong Provincial Key Laboratory of Optical Astronomy and Solar-Terrestrial Environment, Institute of Space Sciences, Shandong University, Weihai 264209, China

² CAS Key Laboratory of Geospace Environment, University of Science & Technology of China, Chinese Academy of Sciences, Hefei 230026, China

2005; Banerjee *et al.*, 2007; Roberts, 2008; De Moortel and Nakariakov, 2012; Liu and Ofman, 2014). When combined with magnetohydrodynamic (MHD) theory, the measured wave parameters allow inferring the solar atmospheric parameters that are difficult to measure directly. This practice was originally proposed for the solar corona (Roberts, Edwin, and Benz, 1984; see also Rosenberg, 1970; Uchida, 1970; Zajtsev and Stepanov, 1975), but has been extended to spicules (*e.g.*, Zaqarashvili and Erdélyi, 2009), prominences (*e.g.*, Arregui, Oliver, and Ballester, 2012), magnetic pores (*e.g.*, Morton *et al.*, 2011), and various structures in the chromosphere (*e.g.*, Jess *et al.*, 2009; Morton *et al.*, 2012), to name but a few. Compared with sausage waves (with azimuthal wavenumber $m = 0$), kink waves (with $m = 1$) have received more attention, presumably because of their ubiquity in the solar atmosphere (*e.g.*, Nakariakov *et al.*, 1999; Aschwanden *et al.*, 1999; Tomczyk and McIntosh, 2009; Kupriyanova, Melnikov, and Shibasaki, 2013). However, recent observations indicated that sausage waves abound as well (*e.g.*, Nakariakov, Melnikov, and Reznikova, 2003; Morton *et al.*, 2012; Grant *et al.*, 2015; Moreels *et al.*, 2015). In addition, standing sausage modes in flare loops were shown to be important for interpreting a considerable fraction of quasi-periodic pulsations (QPPs) in the light curves of solar flares (see Nakariakov and Melnikov (2009) for a recent review).

A theoretical understanding of fast sausage waves supported by magnetized cylinders is crucial for their seismological applications. For this purpose, the transverse density distribution is usually idealized as being in a step-function (top-hat) form, characterized by the internal (ρ_i) and external (ρ_e) values (*e.g.*, Meerson, Sasorov, and Stepanov, 1978; Spruit, 1982; Edwin and Roberts, 1983; Cally, 1986; Kopylova *et al.*, 2007; Vasheghani Farahani *et al.*, 2014). In a low- β environment such as the solar corona, two regimes are known to exist, depending on the longitudinal wavenumber k (*e.g.*, Spruit, 1982). When k exceeds some critical k_c , the trapped regime arises, whereby the sausage wave energy is well confined to the cylinder. In contrast, if $k < k_c$, then the leaky regime results, and fast sausage waves experience apparent temporal damping by emitting their energy into the surrounding fluid. Furthermore, the k -dependence of the periods P and damping times τ of leaky waves disappears when k is sufficiently small (*e.g.*, Kopylova *et al.*, 2007; Vasheghani Farahani *et al.*, 2014). Let R denote the cylinder radius, and v_{Ai} denote the internal Alfvén speed. In the long-wavelength limit ($k \rightarrow 0$), P is found to be primarily determined by the transverse Alfvén transit time R/v_{Ai} , while the ratio τ/P is largely proportional to the density contrast ρ_i/ρ_e (Kopylova *et al.*, 2007). This then enables one to employ the measured P and τ to deduce ρ_i/ρ_e and R/v_{Ai} , with the latter carrying important information on the magnetic field strength in flare loops.

Evidently, there is no reason to expect that the density distribution across magnetic cylinders is in a step-function fashion. This has stimulated a series of studies to examine the properties of fast sausage waves in magnetized cylinders with a continuous transverse density profile by either proceeding analytically with an eigenmode analysis (Edwin and Roberts, 1988; Lopin and Nagorny, 2014, 2015) or numerically solving the linearized MHD equations as an initial-value problem (Nakariakov, Hornsey, and Melnikov, 2012; Chen *et al.*, 2015a). Many features in the step-function case, the k -dependence in particular, were found to survive. However, the period P (Nakariakov, Hornsey, and Melnikov, 2012) and damping time τ (Chen *et al.*, 2015a) may be sensitive to yet another parameter, namely the steepness or equivalently the length scale of the transverse density inhomogeneity. We note that the steepness is crucial in determining such coronal heating mechanisms as resonant absorption (*e.g.*, Hollweg and Yang, 1988; Goossens, Andries, and Aschwanden, 2002; Ruderman and Roberts, 2002) and phase mixing (Heyvaerts and Priest, 1983). There is then an obvious need to employ the measured P and τ of sausage modes to infer the profile steepness, in much

the same way that kink modes were employed (Arregui *et al.*, 2007; Goossens *et al.*, 2008; Soler *et al.*, 2014). This was undertaken by Chen *et al.* (2015b, hereafter Paper I), based on an analytical dispersion relation (DR) governing linear fast sausage waves in cylinders with a rather general transverse density distribution. The only requirement was that this profile can be decomposed into a uniform cord, a uniform external medium, and a transition layer connecting the two. However, this layer can be of arbitrary width and the profile therein can be in arbitrary form.

The aim of the present study is to extend the analysis in Paper I in the following aspects. First, we remove the restriction for the transverse density profile to involve a uniform cord, thereby enabling the analysis to be applicable to a richer variety of density distributions. Second, when validating the results from this eigenmode analysis, we employ an independent approach by solving the time-dependent version of linear MHD equations. We detail these time-dependent computations pertinent to the afore-mentioned transverse density profile. Third, we extend the seismological applications in Paper I to QPP events that involve both kink and sausage modes. To illustrate the scheme for inverting multi-mode measurements, Paper I adopted the analytical expressions for the kink mode period and damping time in the thin-tube-thin-boundary (TTTB) limit as given by Goossens *et al.* (2008). In this study we replace the TTTB expressions with a self-consistent, linear, resistive MHD computation. This is necessary given that flare loops tend not to be thin (Aschwanden, Nakariakov, and Melnikov, 2004), and it is not safe to assume a priori that the density inhomogeneity takes place in a thin transition layer. Fourth, in connection with the third point, we take this opportunity to provide a very detailed examination of resonantly damped kink modes in cylinders with transverse density profiles in question.

This manuscript is organized as follows. Section 2 presents the necessary equations, the derivation of the analytic DR in particular. The behavior of sausage waves in nonuniform cylinders and its applications to QPP events are then presented in Section 3. Finally, Section 4 summarizes the present study.

2. Mathematical Formulation

2.1. Derivation of the Dispersion Relation

Appropriate for the solar corona, we adopted ideal, cold (zero- β) MHD to describe fast sausage waves. The magnetic loops hosting these waves were modeled as straight cylinders with radius R aligned with a uniform magnetic field $\mathbf{B} = B\hat{z}$, where a standard cylindrical coordinate system (r, θ, z) was adopted. The equilibrium density was assumed to be a function of r only and of the form

$$\rho(r) = \begin{cases} \rho_i [1 - (1 - \frac{\rho_e}{\rho_i}) f(r)], & 0 \leq r < R, \\ \rho_e, & r > R, \end{cases} \quad (1)$$

where $f(r)$ is some arbitrary function that increases smoothly from 0 at $r = 0$ to unity when $r = R$. Furthermore, ρ_i and ρ_e denote the densities at the cylinder axis and in the external medium, respectively. The corresponding Alfvén speeds follow from the definition $v_{\text{Ai,e}} = B/\sqrt{4\pi\rho_{\text{i,e}}}$.

It suffices to briefly outline the mathematical approach for establishing the pertinent dispersion relation (DR), since this approach has been detailed in Paper I. To start, we focused on axisymmetric sausage perturbations, and Fourier-analyzed any perturbation $\delta f(r, z, t)$ as

$$\delta f(r, z, t) = \text{Re}\{\tilde{f}(r) \exp[-i(\omega t - kz)]\}. \quad (2)$$

It then follows from the linearized, ideal, cold MHD equations that the Fourier amplitudes of the transverse Lagrangian displacement ($\tilde{\xi}_r$) and Eulerian perturbation of total pressure (\tilde{p}_T) are governed by Equations (6) and (7) in Paper I, respectively. Now that sausage waves do not resonantly couple to torsional Alfvén waves for the configuration we examine, we employed regular series expansions about $y \equiv r - R/2 = 0$ to express $\tilde{\xi}_r$ and \tilde{p}_T in the nonuniform portion of the density distribution. Further requiring that sausage waves do not disturb the cylinder axis ($\tilde{\xi}_r = 0$ at $r = 0$), and employing the conditions for $\tilde{\xi}_r$ and \tilde{p}_T to be continuous at the interface $r = R$, we found that the DR can be expressed as

$$\frac{\frac{\mu_e R H_0^{(1)}(\mu_e R)}{H_1^{(1)}(\mu_e R)} \tilde{\xi}_1(R/2) - \tilde{\xi}_1(R/2) - R \tilde{\xi}'_1(R/2)}{\tilde{\xi}_1(-R/2)} = \frac{\frac{\mu_e R H_0^{(1)}(\mu_e R)}{H_1^{(1)}(\mu_e R)} \tilde{\xi}_2(R/2) - \tilde{\xi}_2(R/2) - R \tilde{\xi}'_2(R/2)}{\tilde{\xi}_2(-R/2)}. \tag{3}$$

Here $H_n^{(1)}$ denotes the n -th order Hankel function of the first kind, and μ_e is defined by

$$\mu_e^2 = \frac{\omega^2}{v_{\text{Ae}}^2} - k^2 \quad \left(-\frac{\pi}{2} < \arg \mu_e \leq \frac{\pi}{2} \right). \tag{4}$$

Furthermore,

$$\tilde{\xi}_1(y) = \sum_{n=0}^{\infty} a_n y^n \quad \text{and} \quad \tilde{\xi}_2(y) = \sum_{n=0}^{\infty} b_n y^n \tag{5}$$

are two linearly independent solutions for $\tilde{\xi}_r$ in the portion $r < R$. Without loss of generality, we chose

$$a_0 = R, \quad a_1 = 0, \quad b_0 = 0, \quad b_1 = 1. \tag{6}$$

The rest of the coefficients a_n and b_n can be found by replacing R with $R/2$ in Equation (11) in Paper I and contain the information on the density distribution. Finally, the prime ' denotes the derivative of $\tilde{\xi}_{1,2}$ with respect to y .

Before proceeding, we note that a series-expansion-based approach was recently adopted by Soler *et al.* (2013) to treat wave modes in transversally nonuniform cylinders where the azimuthal wavenumber m is allowed to be arbitrary. A comparison between this approach and ours is detailed in Appendix C, where we show that both approaches yield identical results for trapped sausage modes ($m = 0$). While our approach seems more appropriate to describe leaky sausage modes, we stress that a singular expansion as employed by Soler *et al.* (2013) is necessary to treat wave modes with $m \neq 0$.

2.2. Solution Method

Throughout this study, we focus on standing sausage modes by restricting longitudinal wavenumbers (k) to be real, but allowing angular frequencies (ω) to be complex-valued ($\omega = \omega_R + i\omega_I$). In addition, we focus on fundamental modes, namely those with $k = \pi/L$ where L is the loop length. In practice, we started with prescribing an $f(r)$, and then solved Equation (3) by truncating the infinite series expansion (Equation (5)) to retain terms with n up to $N = 101$. Using an even larger N leads to no appreciable difference. It should be noted that ω in units of v_{Ai}/R depends only on the combination $[f(r), kR, \rho_1/\rho_e]$. The

corresponding period P and damping time τ follow from the definitions $P = 2\pi/\omega_R$ and $\tau = 1/|\omega_I|$.

For validation purposes, we also obtained ω as a function of k in a way independent of this eigenmode analysis. This was done by solving the time-dependent equation governing the transverse velocity perturbation $\delta v_r(r, z, t)$ as an initial-value problem. For given combinations of $[f(r), kR, \rho_i/\rho_e]$, the periods and damping times of sausage modes can be found by analyzing the temporal evolution of the perturbation signals (see Appendix A for details). As we show in Figure 2, the values of P and τ derived from the two independent approaches are in close agreement. However, numerically solving the analytical DR is much less computationally expensive. In addition, the values of τ for heavily damped modes can be readily found, whereas the perturbation signals in time-dependent computations decay too rapidly to allow a proper determination of τ .

3. Numerical Results

It is impossible to exhaust the possible prescriptions for $f(r)$. We therefore focus on one choice, namely

$$f(r) = \left(\frac{r}{R}\right)^\mu, \tag{7}$$

where μ is positive. The density profiles with a number of different μ are shown in Figure 1, where ρ_i/ρ_e is chosen to be 100 for illustration purposes. Evidently, the profile becomes increasingly steep as μ increases and approaches a step-function form when μ approaches infinity. This makes it possible to investigate the effect of profile steepness by examining the μ -dependence of the numerical results. In addition, for fundamental modes with $k = \pi/L$, the dependence on kR is translated into that on the length-to-radius ratio L/R .

3.1. Behavior of Sausage Waves in Nonuniform Tubes

Figure 2 presents the dependence on L/R of the period P and damping time τ for a series of μ values as labeled. For illustration purposes, the density ratio ρ_i/ρ_e is taken to be 100. The dash-dotted line in Figure 2a represents $P = 2L/v_{Ae}$, and separates trapped (to its left) from leaky (right) modes. The solid curves represent the results from solving the analytical DR (Equation (3)), whereas the circles represent those obtained with the initial-value-problem

Figure 1 Transverse equilibrium density profiles as a function of r for different steepness parameters μ as labeled. Here the density contrast ρ_i/ρ_e is chosen to be 100 for illustration purposes.

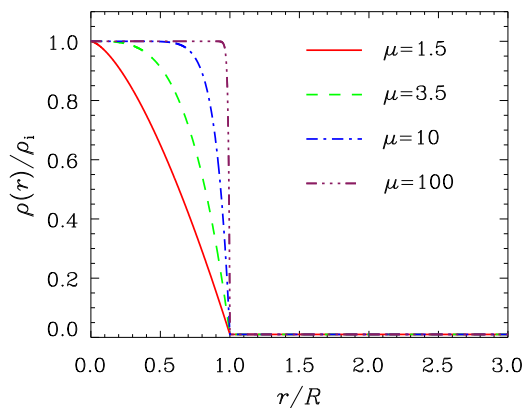
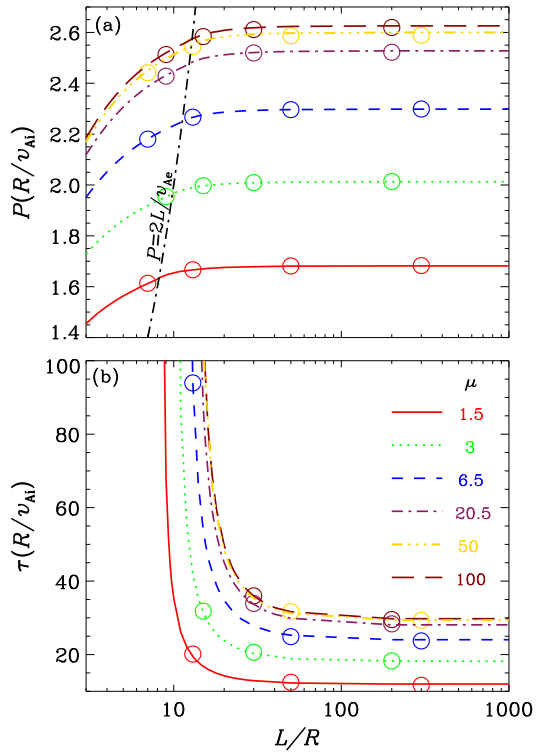


Figure 2 Dependence on length-to-radius ratio L/R of (a) periods P and (b) damping times τ of fundamental sausage modes. A number of density profiles with different μ are examined as labeled. The black dash-dotted line in (a) represents $P = 2L/v_{Ai}$ and separates the trapped (to its left) from leaky (right) regimes. The open circles represent the values obtained by solving Equation (12) with an initial-value-problem approach, which is independent of the eigen-mode analysis presented in the text. The density contrast ρ_i/ρ_e is chosen to be 100.



approach. A close agreement between the curves and circles is clear, thereby validating the DR.

Figure 2a indicates that the wave period P increases monotonically with L/R in the trapped regime and rapidly settles to some asymptotic value in the leaky one. Likewise, Figure 2b shows that, being identically infinite in the trapped regime, the damping time τ also experiences saturation for sufficiently large L/R . In addition, both P and τ increase substantially with increasing μ at a given L/R . We note that while the tendency for P to be larger for steeper density profiles agrees with the study by Nakariakov, Hornsey, and Melnikov (2012), it does not hold in general. Figure 3 in Paper I shows that the opposite occurs for some different profile prescriptions. This means that the largely unknown specific form of the transverse density distribution plays an important role in determining the dispersive properties of sausage modes. Consequently, when the period and damping time of sausage modes are seismologically exploited, the uncertainty in specifying the density profile needs to be considered.

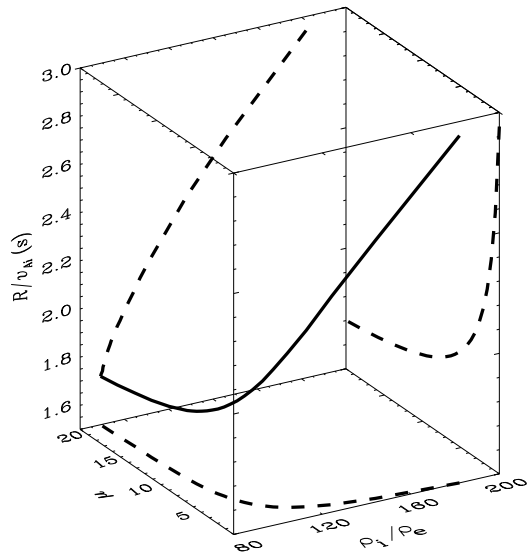
3.2. Applications to Spatially Unresolved QPP Observations

In essence, Figure 2 indicates that the period P and damping time τ of sausage modes can be formally expressed as

$$P_{\text{saus}} = \frac{R}{v_{Ai}} F_{\text{saus}} \left(\frac{L}{R}, \mu, \frac{\rho_i}{\rho_e} \right), \tag{8}$$

$$\frac{\tau_{\text{saus}}}{P_{\text{saus}}} = G_{\text{saus}} \left(\frac{L}{R}, \mu, \frac{\rho_i}{\rho_e} \right). \tag{9}$$

Figure 3 Inversion curve (the solid line) and its projections (dashed) in the three-dimensional parameter space spanned by $[\mu, \rho_i/\rho_e, R/v_{Ai}]$. All points along this curve are equally possible to reproduce the quasi-periodic-pulsation event reported in McLean and Sheridan (1973), where the oscillation period is 4.3 s, and the damping-time-to-period ratio is ten.



We note that the damping-time-to-period ratio τ/P is adopted here instead of τ itself, the reason being that τ/P does not depend on R/v_{Ai} . Furthermore, the L/R -dependence disappears for cylinders with large enough L/R .

We first consider the applications of Equations (8) and (9) to spatially unresolved QPP events, for which only P and/or τ can be regarded known. However, the information is missing on both the physical parameters $[v_{Ai}, \mu, \rho_i/\rho_e]$ and geometrical parameters $[L, R]$. If a trapped sausage mode is responsible for causing a QPP event, which occurs when the signals do not show clear damping, then only Equation (8) is relevant. This means that any point on a three-dimensional (3D) hypersurface in the 4D space formed by $[R/v_{Ai}, L/R, \mu, \rho_i/\rho_e]$ is possible to reproduce the measured P . Even if the signals in a QPP event are temporally decaying, the range of possible parameters that can reproduce the measured P and τ is still too broad to be useful: a 2D surface in the 4D parameter space results. The situation improves if we can assume that the flare loops hosting sausage modes are sufficiently thin such that the L/R -dependence drops out. Equations (8) and (9) then suggest that for trapped (leaky) modes, we can deduce a 2D surface (1D curve) in the 3D space formed by $[R/v_{Ai}, \mu, \rho_i/\rho_e]$. We note that the idea for deriving 1D inversion curves was first introduced by Arregui *et al.* (2007) and later explored in *e.g.*, Goossens *et al.* (2008) and Soler *et al.* (2014). While resonantly damped kink modes were examined therein, the same idea also applies to leaky sausage modes in thin cylinders, the only difference being that the transverse Alfvén time (R/v_{Ai}) replaces the longitudinal one (L/v_{Ai}).

Figure 3 presents the 1D curve and its projections (the dashed lines) onto various planes in the $[R/v_{Ai}, \mu, \rho_i/\rho_e]$ space, using the QPP event reported in McLean and Sheridan (1973) as an example. For this event, the oscillation period is 4.3 s and the damping-time-to-period ratio is ten. Table 1 presents a set of values read from the solid curve in Figure 3. Of the parameters to be inferred, the transverse Alfvén time R/v_{Ai} and density ratio ρ_i/ρ_e can be somewhat constrained. To be specific, the pair $[R/v_{Ai}, \rho_i/\rho_e]$ reads [2.94 s, 182] when $\mu = 1$, and reads [1.64 s, 88.2] when $\mu = 100$. However, the steepness parameter μ is difficult to constrain, since its possible range is too broad. This agrees with Paper I, where we concluded that for spatially unresolved QPPs, the transverse Alfvén time is the best con-

Table 1 Values of $[\mu, \rho_i/\rho_e, R/v_{Ai}]$ deduced for the QPP event reported in McLean and Sheridan (1973).

μ	1	2.5	4	6.5	9	12	20	60	100
ρ_i/ρ_e	182.0	118.3	104.0	95.8	92.5	91.0	89.2	88.2	88.2
R/v_{Ai} (s)	2.94	2.23	2.02	1.87	1.80	1.76	1.7	1.65	1.64

strained, whereas the steepness (the length of the transition layer in units of loop radius l/R in that paper) corresponds to the other extreme.

The question then is how to make sense of this seismological inversion. To this end, we may compare our results with what is found with the DR for a step-function density profile (Equation (18) in Paper I). Noting that the μ -dependence no longer exists in the step-function case, we find with the measured P and τ that $[R/v_{Ai}, \rho_i/\rho_e] = [1.62 \text{ s}, 88.2]$. As expected, this agrees well with what we found for large μ . However, it differs substantially from the results for small μ . From this we conclude that, although simple and straightforward, the practice for deducing $[R/v_{Ai}, \rho_i/\rho_e]$ using the DR for step-function profiles is subject to substantial uncertainty if the uncertainties in prescribing the transverse density structuring are taken into account. In particular, it may substantially underestimate R/v_{Ai} . This uncertainty will be carried over to the deduced values of the Alfvén speed and consequently the magnetic field strength, provided that we can further estimate the loop radius R and internal density ρ_i .

3.3. Applications to Spatially Resolved QPP Observations

We now consider the seismological applications of Equations (8) and (9) to spatially resolved QPP events. In this case, the geometrical parameters L and R can be considered known, and only the combination of $[v_{Ai}, \mu, \rho_i/\rho_e]$ remains to be deduced. It then follows that if a trapped (leaky) mode is presumably the cause of a QPP event, the measured period P (P together with the damping time τ) allows a 2D surface (1D curve) to be found in the 3D space formed by $[v_{Ai}, \mu, \rho_i/\rho_e]$.

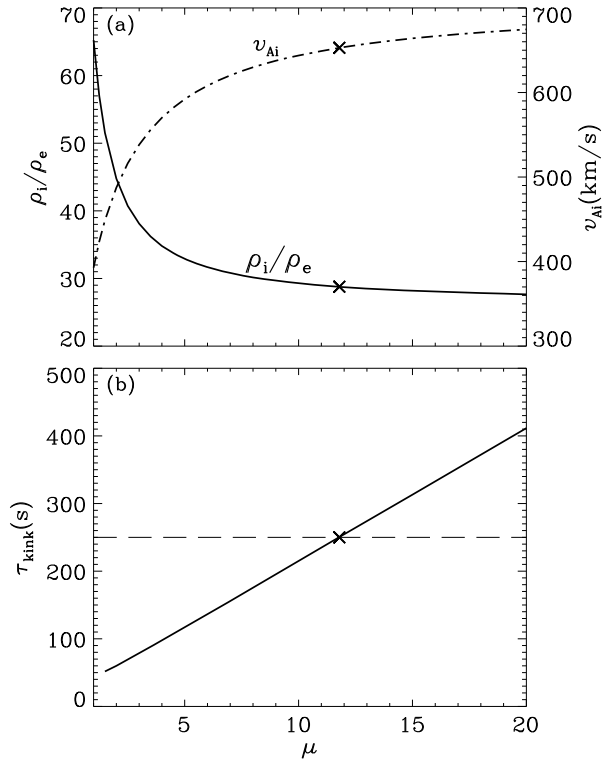
Something more definitive can be deduced if a QPP event involves more than just a sausage mode. Similar to Paper I, we examined the case where a fundamental kink mode exists together with a fundamental sausage one, with both experiencing temporal damping. Let P_{saus} and τ_{saus} denote the period and damping time of the sausage mode, respectively. Likewise, let P_{kink} (τ_{kink}) denote the period (damping time) of the kink mode. Furthermore, we assume that wave leakage leads to the apparent damping of the sausage mode, whereas resonant absorption is responsible for damping the kink mode. We find that P_{kink} and τ_{kink} can be formally expressed as

$$P_{\text{kink}} = \frac{L}{v_{Ai}} F_{\text{kink}} \left(\frac{L}{R}, \mu, \frac{\rho_i}{\rho_e} \right), \tag{10}$$

$$\tau_{\text{kink}} = \frac{L}{v_{Ai}} H_{\text{kink}} \left(\frac{L}{R}, \mu, \frac{\rho_i}{\rho_e} \right). \tag{11}$$

To establish the functions F_{kink} and H_{kink} , we adopted the same approach as in Terradas, Oliver, and Ballester (2006). A set of linearized resistive MHD equations (Equations (1)–(5) therein) was solved for the dimensionless complex angular frequency ($\omega_{\text{kink}}L/v_{Ai}$) as an eigenvalue. A uniform resistivity $\bar{\eta}$ was adopted, resulting in a magnetic Reynolds number $R_m = v_{Ai}R/\bar{\eta}$. It turns out that $\omega_{\text{kink}}L/v_{Ai}$ does not depend on R_m when R_m is sufficiently

Figure 4 Illustration of the scheme for inverting the two-mode QPP event reported in Kolotkov *et al.* (2015). The curves in (a) are found by requiring that the damping-time-to-period ratio $\tau_{\text{saus}}/P_{\text{saus}}$ and period P_{saus} for fundamental sausage modes agree with the measured values for a series of given values of μ . The solid curve in (b) represents the damping time τ_{kink} for fundamental kink modes expected with the values $[\mu, \rho_i/\rho_e, v_{\text{Ai}}]$ given in (a). Its intersection with the horizontal dashed line, representing the measured value for τ_{kink} , gives a unique combination of $[\mu, \rho_i/\rho_e, v_{\text{Ai}}]$ labeled by the crosses.



large, and this saturation value is taken to be the value that $\omega_{\text{kink}}L/v_{\text{Ai}}$ attains with the input parameters $[L/R, \mu, \rho_i/\rho_e]$ (see Appendix B for details). We note that F_{kink} and H_{kink} can also be established with the approach developed by Soler *et al.* (2013), where a less computationally costly method based on singular series expansion was employed.

With $P_{\text{saus}}, \tau_{\text{saus}}, P_{\text{kink}},$ and τ_{kink} measured, we find that the number of equations is more than needed, since now there are only three unknowns, $v_{\text{Ai}}, \mu,$ and ρ_i/ρ_e . In practice, we consider the expression for P_{kink} as redundant and use the rest for seismological purposes. As suggested in Paper I, the kink mode period expected from Equation (10) with the deduced parameters can be compared with the measured value. The difference between the two allows us to say, for instance, whether it is safe to identify the oscillating signals with the particular modes. In addition, this difference can also serve as an estimate of the errors of the deduced loop parameters for a given density prescription.

While seemingly fortuitous, QPP events involving multiple modes do occur (e.g., Nakariakov, Melnikov, and Reznikova, 2003; Kupriyanova, Melnikov, and Shibasaki, 2013; Kolotkov *et al.*, 2015). For instance, when analyzing the multiple signals in the QPP event on 14 May 2013, Kolotkov *et al.* (2015) identified a fundamental fast kink mode with period $P_{\text{kink}} = 100$ s and damping time $\tau_{\text{kink}} = 250$ s together with a fundamental sausage mode with $P_{\text{saus}} = 15$ s and $\tau_{\text{saus}} = 90$ s. In addition, the flare loop hosting the two modes was suggested to be of length $L = 4 \times 10^4$ km and radius $R = 4 \times 10^3$ km, if the apparent width of the loop is taken as the loop diameter. Now the seismological inversion is rather straightforward and involves only two steps, as illustrated in Figure 4. First, with the aid of Equation (9), we readily derive a curve (the solid curve in Figure 4a) in the $[\mu, \rho_i/\rho_e]$ plane to be compatible with the measured $\tau_{\text{saus}}/P_{\text{saus}}$. The internal Alfvén speed v_{Ai} for a given

pair of $[\mu, \rho_i/\rho_e]$ is then found with Equation (8) to agree with the measured P_{saus} , yielding the dash-dotted curve. Second, we evaluate the kink mode damping time with Equation (11) with a series of combinations $[v_{\text{Ai}}, \mu, \rho_i/\rho_e]$, thereby finding the solid curve in Figure 4b. The intersection of this solid curve with the horizontal dashed line, representing the measured kink mode damping time ($\tau_{\text{kink}} = 250$ s), then yields that $\mu = 11.8$, $\rho_i/\rho_e = 28.8$, and $v_{\text{Ai}} = 653 \text{ km s}^{-1}$. It is worth stressing that Equation (10) yields an expected kink mode period of 88 s with the measured L and R as well as this set of deduced parameters. This is close to what was measured (100 s), substantiating the interpretation of the long-period signal as the fundamental kink mode, as was done by Kolotkov *et al.* (2015). Alternatively, this agreement between the two values also suggests that the errors in this inversion procedure are rather moderate.

What are the uncertainties of the derived flare loop parameters? Evidently, they come entirely from the uncertainties associated with the unknown specific form of the transverse density structuring. To provide an uncertainty measure, we repeated the afore-mentioned inversion process for all four different density prescriptions in Paper I, where we examined only one profile (the sine profile) and adopted the TTTB approximation to describe F_{kink} and H_{kink} . Now with the pertinent analytical DRs for sausage modes and self-consistent resistive MHD computations for kink modes, we find that the density contrast ρ_i/ρ_e is constrained to the range from 28.4 to 31.1, and the internal Alfvén speed v_{Ai} lies between 594 and 658 km s^{-1} . Interestingly, for the μ -power profile examined here, the values inferred for ρ_i/ρ_e and v_{Ai} also lie in these rather narrow ranges. On the other hand, the deduced μ value indicates that the density profile across the flare loop in question is rather steep, which also agrees with the ratios of the transition layer width to loop radius ($0.167 \leq l/R \leq 0.284$) inferred with the profile prescriptions in Paper I. From this we conclude that at least for the profiles examined in the present study and Paper I, the uncertainties of the inferred profile steepness, density contrast, and internal Alfvén speed are relatively small.

4. Summary

A substantial fraction of quasi-periodic pulsations (QPPs) in the light curves of solar flares is attributed to sausage modes in flare loops. The present study continues the effort we initiated in Chen *et al.* (2015b, Paper I) to infer flare loop parameters with the measured periods P and damping times τ of fundamental standing sausage modes supported therein. For this purpose we extended the analysis of Paper I to sausage waves in nonuniform, straight, coronal cylinders with arbitrary transverse density profiles comprising a nonuniform inner portion and a uniform external medium. Working in the framework of ideal and cold MHD, we derived an analytical dispersion relation (DR, Equation (3)) and focused on density profiles of a μ -power form (Equation (7)). The dispersive properties of fundamental standing modes were examined, together with their potential to infer flare loop parameters.

We found that P and τ in units of the transverse Alfvén time R/v_{Ai} depend only on the density contrast ρ_i/ρ_e , length-to-radius ratio L/R of coronal cylinders, and the profile steepness μ . For all profiles examined in both this study and Paper I, when the rest of the parameters are fixed, P (τ) in units of R/v_{Ai} increases (decreases) with increasing L/R and tends to some saturation value when L/R is sufficiently large. For spatially unresolved QPPs, we showed that a curve in the 3D space formed by R/v_{Ai} , ρ_i/ρ_e , and μ can almost be deduced. This occurs when we can assume that $L/R \gg 1$ beforehand. Applying this inversion procedure to the event reported by McLean and Sheridan (1973), we found that R/v_{Ai} is the best constrained, whereas the steepness parameter is the least constrained. For spatially

resolved QPPs, we showed that while geometric parameters of flare loops are available, the inversion problem remains under-determined. However, when an additional mode co-exists with the fundamental sausage mode, the full information on the unknowns, $[v_{Ai}, \mu, \rho_i/\rho_e]$, can be inferred. In this case, the inversion problem may become over-determined. Applying this idea to a recent QPP event where temporally decaying kink and sausage modes were identified, we found that v_{Ai} , ρ_i/ρ_e , and the profile steepness can be constrained to rather narrow ranges.

The discussions on the limitations to our inversion procedures as presented in Paper I also apply here and are not repeated. Instead, we stress the great potential of using multi-mode QPP measurements to determine flare loop parameters rather precisely, the internal Alfvén speed in particular. To this end, not only modes of distinct nature (*e.g.*, a fundamental kink mode co-existing with a sausage one) are useful, modes of the same nature but with different longitudinal node numbers work as well. While fundamental kink modes and their harmonics have been seismologically exploited (see *e.g.*, the review by Andries *et al.*, 2009), serious studies using sausage modes need to be conducted.

Before closing, we note that Bayesian techniques have been successfully applied to the inference of density structuring transverse to coronal loops hosting resonantly damping kink modes (Asensio Ramos and Arregui, 2013; Arregui, Asensio Ramos, and Pascoe, 2013; Arregui, Soler, and Asensio Ramos, 2015). With such techniques, the errors in the measurements of kink mode periods and damping times can be properly propagated, and the plausibility of a density profile prescription can be assessed. When no particular prescription is favored, approaches like model-averaging can be employed to yield an evidence-averaged inference. While so far the applications of such techniques have been primarily focused on kink modes, similar ideas are expected to be equally applicable to sausage modes. For this purpose, the DRs derived here and in Paper I should be useful.

Acknowledgements We thank the referee, R. Soler, for his constructive comments that substantially helped to improve this manuscript. This research is supported by the 973 program 2012CB825601, National Natural Science Foundation of China (41174154, 41274176, 41274178, and 41474149), the Provincial Natural Science Foundation of Shandong via Grant JQ201212, and also by a special fund of Key Laboratory of Chinese Academy of Sciences.

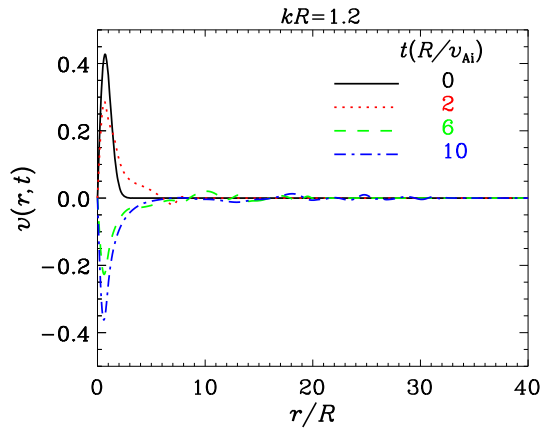
Appendix A: Fast Sausage Modes in Nonuniform Cylinders: A Time-Dependent Approach

This section provides a detailed examination of sausage modes from an initial-value-problem perspective. We note that similar studies were carried out for step-function density profiles by Terradas, Andries, and Goossens (2007), and for continuous profiles by Nakariakov, Hornsey, and Melnikov (2012) and Chen *et al.* (2015a). To start, it is straightforward to derive an equation governing the transverse velocity perturbation $\delta v_r(r, z, t)$ from linearized, time-dependent, cold MHD equations. Formally expressing $\delta v_r(r, z, t)$ as $v(r, t) \sin(kz)$, we find that $v(r, t)$ is governed by (*e.g.*, Chen *et al.*, 2015a)

$$\frac{\partial^2 v(r, t)}{\partial t^2} = v_A^2(r) \left[\frac{\partial^2}{\partial r^2} + \frac{1}{r} \frac{\partial}{\partial r} - \left(\frac{1}{r^2} + k^2 \right) \right] v(r, t). \quad (12)$$

With a $\rho(r)$ profile given by Equations (1) and (7), we can readily evaluate the profile for the Alfvén speed $v_A(r) = B/\sqrt{4\pi\rho(r)}$. Equation (12) can then be readily solved when supplemented with appropriate initial and boundary conditions. For this purpose, we developed

Figure 5 Spatial distribution of the transverse velocity perturbation at a number of different times for $kR = 1.2$. The initial perturbation is described by Equation (13). Here the density ratio $\rho_i/\rho_e = 10$ and the steepness parameter $\mu = 3$.



a simple finite-difference code that is second-order accurate in both space and time, and solved Equation (12) on a uniform grid spanning $[0, r_{\text{outer}}]$ with a spacing $\Delta r = 0.02R$ and $r_{\text{outer}} = 1000R$. A uniform time-step $\Delta t = 0.8\Delta r/v_{\text{Ae}}$ is adopted to ensure numerical stability in view of the Courant condition. We made sure that further refining the grid leads to no discernible difference. Furthermore, the outer boundary r_{outer} is placed sufficiently far from the cylinder such that the signals to be analyzed are not contaminated by the perturbations reflected off the outer boundary. Pertinent to sausage modes, we require that $v(r = 0, t) = 0$. In addition, $v(r = r_{\text{outer}}, t)$ is specified to be zero for simplicity. Throughout this section, we examine a density ratio ρ_i/ρ_e of ten and a steepness parameter μ of three. Moreover, for all computations we adopt the same initial condition (IC)

$$v(r, t = 0) = \frac{r}{R} \exp\left[-\left(\frac{r}{R}\right)^2\right], \quad \frac{\partial}{\partial t} v(r, t = 0) = 0, \tag{13}$$

which is chosen not to be too localized to avoid exciting higher order modes.

Figure 5 presents the spatial distribution of $v(r, t)$ for $kR = 1.2$ at a number of t as labeled. As time progresses, some ripples propagate outward with the external Alfvén speed ($v_{\text{Ae}} = \sqrt{\rho_i/\rho_e}v_{\text{Ai}} = \sqrt{10}v_{\text{Ai}}$). The amplitudes of these ripples are rather insignificant and decrease with time, meaning that little energy is transmitted into the external medium for the adopted IC, even though it is not an exact eigen-function. The majority of the energy is trapped in the cylinder, a signature of trapped modes.

That this computation pertains to the trapped regime is better shown by Figure 6, where the temporal evolution of $v(R, t)$ is displayed. In addition to the numerical results (the black curve), a fit in the form $A \cos(\omega_R t + \phi)$ is given by the red line. This fitting procedure yields that $\omega_R = 3.51v_{\text{Ai}}/R$, in exact agreement with the value found from solving the dispersion relation (Equation (3)). The black curve can be hardly told apart from the red one when $t \gtrsim 4R/v_{\text{Ai}}$, meaning that the signal at this location rapidly evolves into a trapped eigenmode.

What happens for a small kR ? This is examined in Figure 7, where the spatial dependence of $v(r, t)$ for $kR = 0.1$ is presented. In response to the initial perturbation, some ripples are also seen to propagate away from the cylinder. However, in this case the signal close to the cylinder axis ($r = 0$) decays so rapidly that a different scale has to be used to plot $v(r, t)$ at long times (Figure 7b). From Figure 7b we also see that at a given time, the amplitude of the perturbations in the external medium tends to increase with distance first before decreasing

Figure 6 Temporal evolution of the transverse velocity perturbation $v(r = R, t)$ for $kR = 1.2$. The initial perturbation is described by Equation (13). In addition to the numerical result from this time-dependent computation (the black curve), a fit to this curve in the form $A \cos(\omega_R t + \phi)$ is given by the red line for comparison. Here the density ratio $\rho_i/\rho_e = 10$ and the steepness parameter $\mu = 3$.

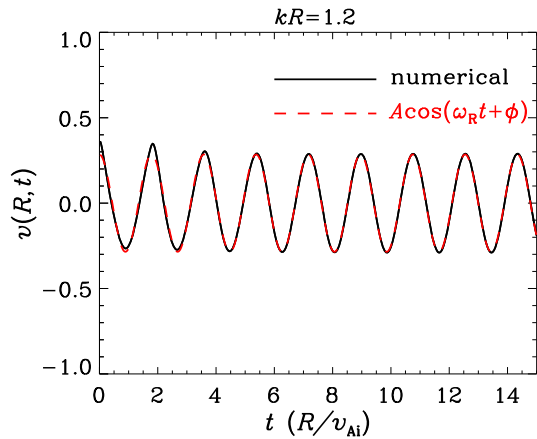
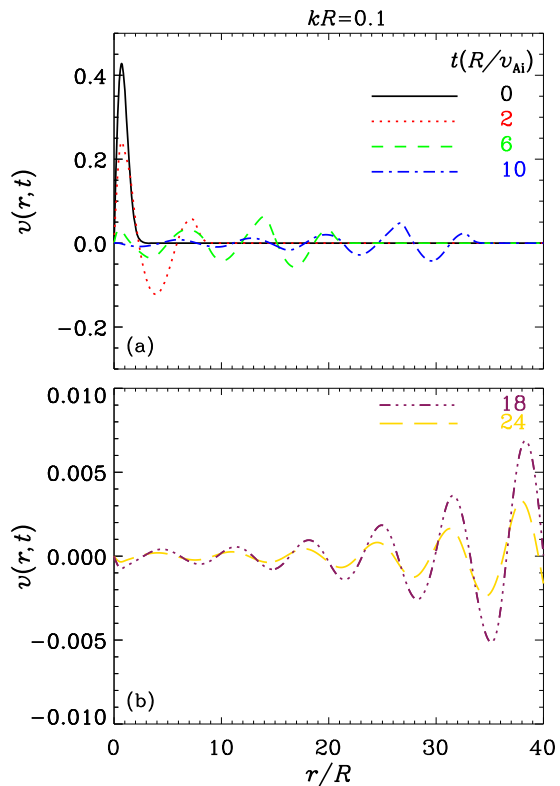


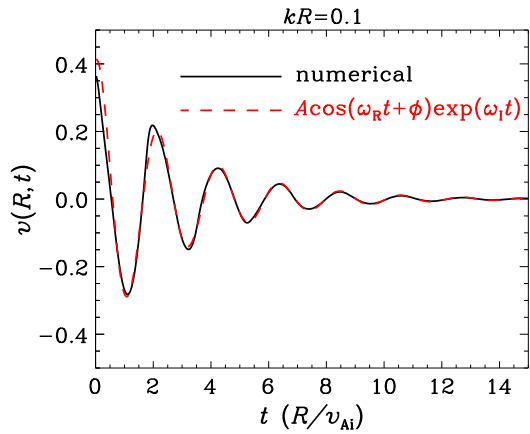
Figure 7 Similar to Figure 5, but for $kR = 0.1$. The spatial distributions for $t = 18$ and $24R/v_{Ai}$ are plotted in a separate panel.



toward the front (also see the blue curve in Figure 7a). This is a signature of leaky eigenfunctions (e.g., Cally, 1986; Terradas, Andries, and Goossens, 2007).

Figure 8 presents the temporal evolution of $v(R, t)$ (the black curve) together with a fitting in the form $A \cos(\omega_R t + \phi) \exp(\omega_I t)$ (red). From this fitting we find that $[\omega_R, \omega_I] = [2.98, -0.34]v_{Ai}/R$, coinciding with the eigenmode computation for the adopted kR . The

Figure 8 Similar to Figure 6, but for $kR = 0.1$. The fit (the red curve) to the time-dependent solution (black) is in the form $A \cos(\omega_R t + \phi) \exp(\omega_I t)$.



black and red curves agree closely with each other for $t \gtrsim 2.5R/v_{Ai}$, substantiating the interpretation that the signal settles to a leaky eigenmode.

Appendix B: Fast Kink Modes in Nonuniform Cylinders: A Resistive, Linear MHD Computation

This section provides some details for the resistive, linear MHD computations that we employed to establish the functions F_{kink} and H_{kink} contained in Equations (10) and (11). Such a description seems informative even though our approach is identical to the one adopted by Terradas, Oliver, and Ballester (2006, hereafter TOB06), since the density profile given by Equation (1) has not been explored for resonantly damped kink modes. Now that the approach has been detailed in Section 3.1 in TOB06, it suffices to note here that we are looking for a dimensionless complex-valued angular frequency $\omega_{\text{kink}}L/v_{Ai}$ for a set of dimensionless parameters $[L/R, \mu, \rho_i/\rho_e]$. The magnetic Reynolds number $R_m = v_{Ai}R/\bar{\eta}$ is also relevant, where $\bar{\eta}$ is the resistivity and assumed to be uniform.

Figure 9 presents the R_m dependence of the real (ω_R) and imaginary (ω_I) parts of the dimensionless angular frequency for $kR = 0.1\pi$ and $\rho_i/\rho_e = 20$. A number of μ values are examined as given by the curves in different colors. Figure 9b shows that the curves significantly depend on R_m only for relatively small R_m . As discussed in TOB06, this is attributable to the competition between resistivity and resonant absorption in damping the kink modes. For large (small) R_m , resonant absorption (resistivity) plays a more important role, and consequently the damping rate $|\omega_I|$ is insensitive (sensitive) to R_m . Interestingly, in agreement with Figure 2 of TOB06, $|\omega_I|$ is not sensitive to the density profile steepness when R_m is small. On the other hand, $|\omega_I|$ rapidly settles to some asymptotic value when R_m exceeds some critical value. Similar to TOB06, with increasing profile steepness this critical R_m increases, whereas the asymptotic $|\omega_I|$ decreases. Examining Figure 9a, we find that ω_R is different for different μ values even at small R_m . Despite this, it is important for the present purpose that neither ω_R nor ω_I depends on R_m when R_m is sufficiently large. Their asymptotic values are taken to be the eigen-frequencies of kink modes whose damping is solely due to resonant absorption.

How do these saturation values depend on the steepness parameter μ when the rest of the parameters are fixed? This is examined in Figure 10, where a series of computations are

Figure 9 Dependence on the magnetic Reynolds number R_m of (a) the real and (b) imaginary parts of the dimensionless eigen-frequency for kink modes in cylinders with a transverse density profile given by Equations (1) and (7). A number of different steepness parameters μ are examined as labeled. Here the dimensionless longitudinal wavenumber $kR = 0.1\pi$, and the density ratio ρ_i/ρ_e is fixed at 20.

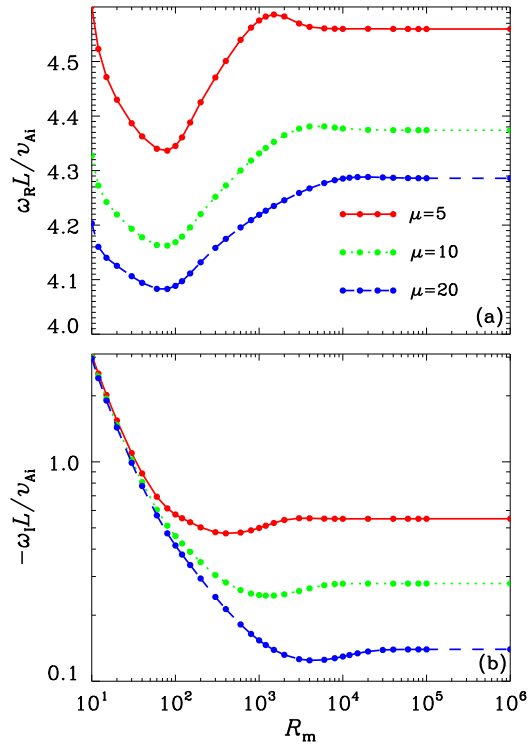
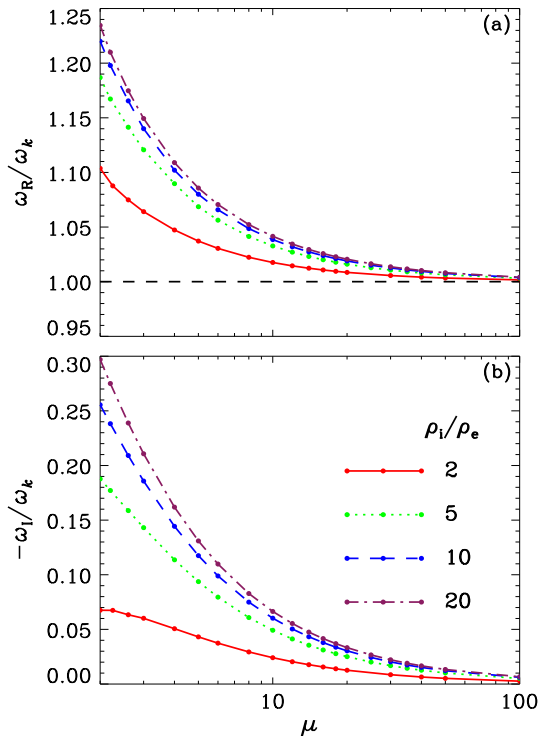


Figure 10 Dependence on the steepness parameter μ of (a) the real and (b) imaginary parts of the eigen-frequencies for resonantly damped kink modes in cylinders with a transverse density profile given by Equations (1) and (7). A number of density ratios ρ_i/ρ_e are examined as labeled. Here the dimensionless longitudinal wavenumber $kR = 0.1\pi$. The eigen-frequencies are found with linear resistive MHD computations at sufficiently large magnetic Reynolds numbers. They are normalized to ω_k , the value attained for density profiles of a step-function form. See text for details.



conducted for a number of density ratios ρ_i/ρ_e as labeled. The dimensionless longitudinal wavenumber kR is also taken to be 0.1π . For presentation purposes, both ω_R and ω_I are normalized to the kink frequency ω_k , which is attained for density profiles of a step-function form. It turns out that the correction to ω_k due to dispersion is not negligible at the chosen kR , meaning that ω_k needs to be computed by solving the relevant dispersion relation (e.g., Edwin and Roberts, 1983, Equation (8b)). The computed value is a few percent different from its thin-tube counterpart, namely $\sqrt{2}kv_{Ai}/\sqrt{1+\rho_e/\rho_i}$ (e.g., Equation (40) in Soler *et al.*, 2013, hereafter S13). Similar to Figure 1 in S13, our Figure 10 shows that ω_R and $|\omega_I|$ tend to decrease with increasing density profile steepness, approaching the step-function values when μ is sufficiently large. In addition, $|\omega_I|/\omega_k$ at a fixed steepness parameter increases with increasing ρ_i/ρ_e . However, while here ω_R/ω_k tends to increase with ρ_i/ρ_e regardless of μ , it does not show a monotonical dependence on ρ_i/ρ_e in Figure 1 of S13 when the steepness parameter is fixed. This difference signifies the importance of describing the density profile in detail when determining the properties of resonantly damped kink modes: while a μ -power profile is examined here, S13 explored a sine profile (Equation (63) therein).

Appendix C: Examining Sausage Modes in Nonuniform Cylinders with Series-Expansion-Based Methods

So far, two series-expansion-based methods have been available to derive explicit expressions for the sausage perturbations in the nonuniform portion of the density distribution. One (approach I, S13) is based on singular expansions as a byproduct of a comprehensive examination of resonantly damped kink modes, whereas the other (approach II, Paper I) is based on regular expansions. This section provides a rather detailed comparison between the two.

To facilitate this comparison, we focus on density profiles considered by both studies, where a transition layer (TL) connects a uniform cord (with density ρ_i) and a uniform external medium (with density ρ_e). The TL is of width l and centered around $r = R$. Approach I solves the perturbation equation (Equation (4) in S13) by conducting an expansion about the Alfvén resonance r_A where $\omega_R = kv_A$. For the density profiles in question, r_A is located in the TL. Valid for arbitrary azimuthal wavenumbers m , the analysis in S13 yields that for sausage modes ($m = 0$), the series solutions are regular even though r_A is a regular singular point. Physically, this means that sausage modes do not resonantly couple to the Alfvén continuum. Approach II capitalizes on this fact and solves the perturbation equation (Equation (6) in Paper I) by performing a regular series expansion about $r = R$. In this aspect, approach II is equivalent to I and both should yield identical solutions, provided that a point exists in the TL such that $\omega_R = kv_A$. Let r_A denote this point for brevity, although it is not a resonance for sausage modes.

Before proceeding, we note that the perturbations in the external medium were required to be evanescent by S13, since leaky modes were not of interest therein. Consequently, the Fourier amplitude of the Eulerian perturbation of total pressure was expressed with $K_0(k_{\perp,e}r)$, the modified Bessel function of the first kind (Equation (10) in S13). To account for leaky sausage modes, this needs to be replaced with $H_0^{(1)}(\mu_e r)$ (e.g., Cally, 1986). Here μ_e is defined by Equation (4), and by definition, $\mu_e^2 = -k_{\perp,e}^2$. With the notations in S13, the

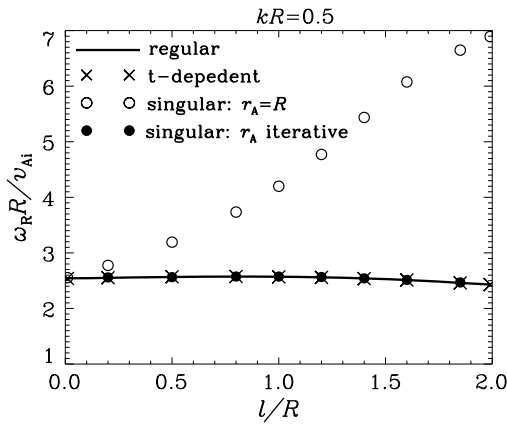


Figure 11 Comparison of two series-expansion-based methods for computing eigen-frequencies of sausage modes. To facilitate this comparison, the density distribution is different from the one described by Equation (1). Instead, the profile labeled “linear” in Equation (4) of Paper I is adopted. Here the dimensionless longitudinal wavenumber $kR = 0.5$, pertinent to the trapped regime ($\omega_I = 0$) for the chosen density ratio ρ_i/ρ_e of 100. The real part of the eigen-frequency ω_R is displayed as a function of l/R , the density length-scale in units of loop radius. The black curve represents the results found with the method based on regular expansions, and the crosses represent those obtained with analyzing the perturbation signals in the corresponding time-dependent computations. Two treatments are adopted for the method based on singular expansions. In one treatment the location of the nominal Alfvén resonance r_A is assumed to be R (the open dots), while in the other it is found iteratively (filled). See text for details.

DR therein then reads

$$\frac{\frac{-\mu_e}{\rho_e(\omega^2 - k^2 v_{A,e}^2)} \frac{H_1^{(1)}[\mu_e(R+l/2)]}{H_0^{(1)}[\mu_e(R+l/2)]} \mathcal{G}_e - \Xi_e}{\frac{-\mu_e}{\rho_e(\omega^2 - k^2 v_{A,e}^2)} \frac{H_1^{(1)}[\mu_e(R+l/2)]}{H_0^{(1)}[\mu_e(R+l/2)]} \mathcal{F}_e - \Gamma_e} = \frac{\frac{-k_{\perp,i}}{\rho_i(\omega^2 - k^2 v_{A,i}^2)} \frac{J_1[k_{\perp,i}(R-l/2)]}{J_0[k_{\perp,i}(R-l/2)]} \mathcal{G}_i - \Xi_i}{\frac{-k_{\perp,i}}{\rho_i(\omega^2 - k^2 v_{A,i}^2)} \frac{J_1[k_{\perp,i}(R-l/2)]}{J_0[k_{\perp,i}(R-l/2)]} \mathcal{F}_i - \Gamma_i} = 0. \tag{14}$$

For non-leaky waves, this recovers Equation (27) in S13, given that

$$\frac{\mu_e H_1^{(1)}[\mu_e(R+l/2)]}{H_0^{(1)}[\mu_e(R+l/2)]} = \frac{k_{\perp,e} K_1[k_{\perp,e}(R+l/2)]}{K_0[k_{\perp,e}(R+l/2)]},$$

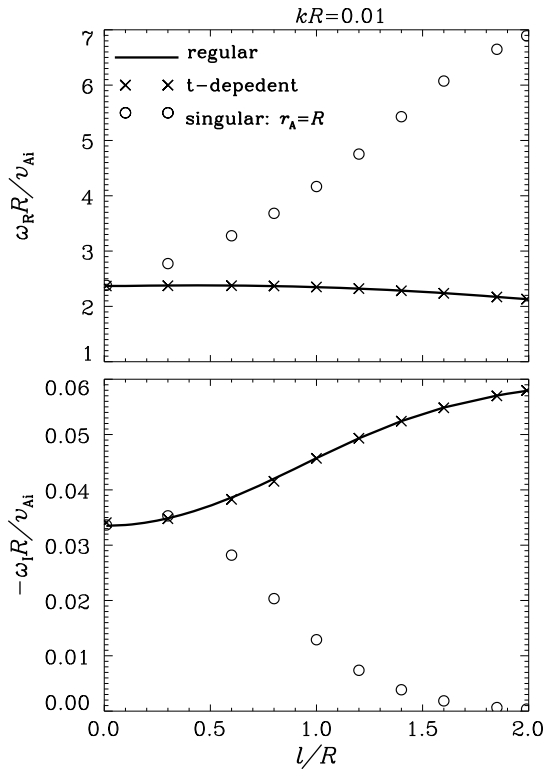
where we have used the relation (Abramowitz and Stegun, 1970)

$$K_m(w) = \frac{\pi}{2} i^{m+1} H_m^{(1)}(iw) \quad \left(-\pi < \arg w \leq \frac{\pi}{2}, m = 0, 1, \dots \right).$$

For illustration purposes, below we examine a linear profile for the density distribution in the TL (Equation (4) in Paper I), and assume that $\rho_i/\rho_e = 100$. For approach I, we solve Equation (14) instead of Equation (27) in S13, and for approach II we solve our Equation (17) in Paper I.

Figure 11 compares the eigen-frequencies found for a series of l/R from the two approaches when kR equals 0.5. This kR falls into the trapped regime since the imaginary parts (ω_I) of the eigen-frequencies are zero, and hence only the real parts (ω_R) are shown. The solid line labeled “regular” represents the solutions from approach II. When adopting approach I, we examine two different treatments for the location of r_A : in one we simply

Figure 12 Similar to Figure 11, but for $kR = 0.01$ pertinent to leaky modes, for which ω_I is non-zero and displayed in a separate panel. See text for details.



take r_A to be R (the open dots), whereas in the other we solve Equation (14) iteratively to simultaneously derive ω_R and r_A (the filled dots). We note that a value for r_A needs to be specified before solving this DR. However, the Alfvén speed at this guessed location usually is not equal to ω_R/k thus found. Hence this latter iterative treatment. The filled dots fall on the solid curve, and both agree exactly with the crosses representing the values found from fitting the signals $v(R, t)$ in the corresponding time-dependent computations (see Appendix A). This means that both approaches yield correct results, and approach II can be seen as a specific case of the more general analysis presented in S13. Nonetheless, the advantage of approach II is that there is no need to find r_A , which is necessary for approach I, given that simply assuming $r_A = R$ beforehand can yield considerably different results (see the open dots).

Some considerable difference arises when leaky sausage modes are examined. We consider $kR = 0.01$, for which the real (ω_R) and imaginary (ω_I) parts of the complex-valued eigen-frequencies are presented in Figure 12. The results from approach II are given by the solid line and are found to agree well with the values found from analyzing the time-dependent results (the crosses). However, they differ substantially from the results found with approach I, where we assumed that $r_A = R$. In this case, the iterative treatment does not work because no point in the TL corresponds to a v_A that equals ω_R/k . The reason is that in the leaky regime the apparent phase speed ω_R/k consistently exceeds v_{Ac} , which in turn always exceeds the Alfvén speeds in the TL.

Despite the afore-mentioned discussions, we stress that the mathematical approach presented in S13 is sufficiently general to treat modes with arbitrary azimuthal wavenumber m ,

trapped sausage modes ($m = 0$) included. A singular series expansion is necessary for treating all modes with $m \neq 0$.

References

- Abramowitz, M., Stegun, I.A.: 1970, *Handbook of Mathematical Functions: With Formulas, Graphs, and Mathematical Tables*, US Dept. of Commerce, National Bureau of Standards, Washington, 375. [ADS](#).
- Andries, J., van Doorselaere, T., Roberts, B., Verth, G., Verwichte, E., Erdélyi, R.: 2009, Coronal seismology by means of kink oscillation overtones. *Space Sci. Rev.* **149**, 3. [DOI](#). [ADS](#).
- Arregui, I., Asensio Ramos, A., Pascoe, D.J.: 2013, Determination of transverse density structuring from propagating magnetohydrodynamic waves in the solar atmosphere. *Astrophys. J. Lett.* **769**, L34. [DOI](#). [ADS](#).
- Arregui, I., Oliver, R., Ballester, J.L.: 2012, Prominence oscillations. *Living Rev. Solar Phys.* **9**, 2. [DOI](#). [ADS](#).
- Arregui, I., Soler, R., Asensio Ramos, A.: 2015, Model comparison for the density structure across solar coronal waveguides. *Astrophys. J.* **811**, 104. [DOI](#). [ADS](#).
- Arregui, I., Andries, J., Van Doorselaere, T., Goossens, M., Poedts, S.: 2007, MHD seismology of coronal loops using the period and damping of quasi-mode kink oscillations. *Astron. Astrophys.* **463**, 333. [DOI](#). [ADS](#).
- Aschwanden, M.J., Nakariakov, V.M., Melnikov, V.F.: 2004, Magnetohydrodynamic sausage-mode oscillations in coronal loops. *Astrophys. J.* **600**, 458. [DOI](#). [ADS](#).
- Aschwanden, M.J., Fletcher, L., Schrijver, C.J., Alexander, D.: 1999, Coronal loop oscillations observed with the Transition Region and Coronal Explorer. *Astrophys. J.* **520**, 880. [DOI](#). [ADS](#).
- Asensio Ramos, A., Arregui, I.: 2013, Coronal loop physical parameters from the analysis of multiple observed transverse oscillations. *Astron. Astrophys.* **554**, A7. [DOI](#). [ADS](#).
- Banerjee, D., Erdélyi, R., Oliver, R., O'Shea, E.: 2007, Present and future observing trends in atmospheric magnetoseismology. *Solar Phys.* **246**, 3. [DOI](#). [ADS](#).
- Cally, P.S.: 1986, Leaky and non-leaky oscillations in magnetic flux tubes. *Solar Phys.* **103**, 277. [DOI](#). [ADS](#).
- Chen, S.-X., Li, B., Xia, L.-D., Yu, H.: 2015a, Periods and damping rates of fast sausage oscillations in multishelled coronal loops. *Solar Phys.* **290**, 2231. [DOI](#). [ADS](#).
- Chen, S.-X., Li, B., Xiong, M., Yu, H., Guo, M.-Z.: 2015b, Standing sausage modes in nonuniform magnetic tubes: an inversion scheme for inferring flare loop parameters. *Astrophys. J.* **812**, 22. [DOI](#). [ADS](#).
- De Moortel, I., Nakariakov, V.M.: 2012, Magnetohydrodynamic waves and coronal seismology: an overview of recent results. *Phil. Trans. Roy. Soc. London A* **370**, 3193. [DOI](#). [ADS](#).
- Edwin, P.M., Roberts, B.: 1983, Wave propagation in a magnetic cylinder. *Solar Phys.* **88**, 179. [DOI](#). [ADS](#).
- Edwin, P.M., Roberts, B.: 1988, Employing analogies for ducted MHD waves in dense coronal structures. *Astron. Astrophys.* **192**, 343. [ADS](#).
- Goossens, M., Andries, J., Aschwanden, M.J.: 2002, Coronal loop oscillations. An interpretation in terms of resonant absorption of quasi-mode kink oscillations. *Astron. Astrophys.* **394**, L39. [DOI](#). [ADS](#).
- Goossens, M., Arregui, I., Ballester, J.L., Wang, T.J.: 2008, Analytic approximate seismology of transversely oscillating coronal loops. *Astron. Astrophys.* **484**, 851. [DOI](#). [ADS](#).
- Grant, S.D.T., Jess, D.B., Moreels, M.G., Morton, R.J., Christian, D.J., Giagkiozis, I., Verth, G., Fedun, V., Keys, P.H., Van Doorselaere, T., Erdélyi, R.: 2015, Wave damping observed in upwardly propagating sausage-mode oscillations contained within a magnetic pore. *Astrophys. J.* **806**, 132. [DOI](#). [ADS](#).
- Heyvaerts, J., Priest, E.R.: 1983, Coronal heating by phase-mixed shear Alfvén waves. *Astron. Astrophys.* **117**, 220. [ADS](#).
- Hollweg, J.V., Yang, G.: 1988, Resonance absorption of compressible magnetohydrodynamic waves at thin 'surfaces'. *J. Geophys. Res.* **93**, 5423. [DOI](#). [ADS](#).
- Jess, D.B., Mathioudakis, M., Erdélyi, R., Crockett, P.J., Keenan, F.P., Christian, D.J.: 2009, Alfvén waves in the lower solar atmosphere. *Science* **323**, 1582. [DOI](#). [ADS](#).
- Kolotkov, D.Y., Nakariakov, V.M., Kupriyanova, E.G., Ratcliffe, H., Shibasaki, K.: 2015, Multi-mode quasi-periodic pulsations in a solar flare. *Astron. Astrophys.* **574**, A53. [DOI](#). [ADS](#).
- Kopylova, Y.G., Melnikov, A.V., Stepanov, A.V., Tsap, Y.T., Goldvarg, T.B.: 2007, Oscillations of coronal loops and second pulsations of solar radio emission. *Astron. Lett.* **33**, 706. [DOI](#). [ADS](#).
- Kupriyanova, E.G., Melnikov, V.F., Shibasaki, K.: 2013, Spatially resolved microwave observations of multiple periodicities in a flaring loop. *Solar Phys.* **284**, 559. [DOI](#). [ADS](#).
- Liu, W., Ofman, L.: 2014, Advances in observing various coronal EUV waves in the SDO era and their seismological applications (Invited review). *Solar Phys.* **289**, 3233. [DOI](#). [ADS](#).
- Lopin, I., Nagorny, I.: 2014, Fast-sausage oscillations in coronal loops with smooth boundary. *Astron. Astrophys.* **572**, A60. [DOI](#). [ADS](#).

- Lopin, I., Nagorny, I.: 2015, Sausage waves in transversely nonuniform monolithic coronal tubes. *Astrophys. J.* **810**, 87. DOI. ADS.
- McLean, D.J., Sheridan, K.V.: 1973, A damped train of regular metre-wave pulses from the Sun. *Solar Phys.* **32**, 485. DOI. ADS.
- Meerson, B.I., Sasorov, P.V., Stepanov, A.V.: 1978, Pulsations of type IV solar radio emission – The bounce-resonance effects. *Solar Phys.* **58**, 165. DOI. ADS.
- Moreels, M.G., Van Doorselaere, T., Grant, S.D.T., Jess, D.B., Goossens, M.: 2015, Energy and energy flux in axisymmetric slow and fast waves. *Astron. Astrophys.* **578**, A60. DOI. ADS.
- Morton, R.J., Erdélyi, R., Jess, D.B., Mathioudakis, M.: 2011, Observations of sausage modes in magnetic pores. *Astrophys. J. Lett.* **729**, L18. DOI. ADS.
- Morton, R.J., Verth, G., Jess, D.B., Kuridze, D., Ruderman, M.S., Mathioudakis, M., Erdélyi, R.: 2012, Observations of ubiquitous compressive waves in the Sun's chromosphere. *Nature Commun.* **3**, 1315. DOI. ADS.
- Nakariakov, V.M., Melnikov, V.F.: 2009, Quasi-periodic pulsations in solar flares. *Space Sci. Rev.* **149**, 119. DOI. ADS.
- Nakariakov, V.M., Verwichte, E.: 2005, Coronal waves and oscillations. *Living Rev. Solar Phys.* **2**, 3. DOI. ADS.
- Nakariakov, V.M., Hornsey, C., Melnikov, V.F.: 2012, Sausage oscillations of coronal plasma structures. *Astrophys. J.* **761**, 134. DOI. ADS.
- Nakariakov, V.M., Melnikov, V.F., Reznikova, V.E.: 2003, Global sausage modes of coronal loops. *Astron. Astrophys.* **412**, L7. DOI. ADS.
- Nakariakov, V.M., Ofman, L., Deluca, E.E., Roberts, B., Davila, J.M.: 1999, TRACE observation of damped coronal loop oscillations: implications for coronal heating. *Science* **285**, 862. DOI. ADS.
- Roberts, B.: 2008, Progress in coronal seismology. In: Erdélyi, R., Mendoza-Briceno, C.A. (eds.) *Waves & Oscillations in the Solar Atmosphere: Heating and Magneto-Seismology*, IAU Symp. **247**, 3. DOI. ADS.
- Roberts, B., Edwin, P.M., Benz, A.O.: 1984, On coronal oscillations. *Astrophys. J.* **279**, 857. DOI. ADS.
- Rosenberg, H.: 1970, Evidence for MHD pulsations in the solar corona. *Astron. Astrophys.* **9**, 159. ADS.
- Ruderman, M.S., Roberts, B.: 2002, The damping of coronal loop oscillations. *Astrophys. J.* **577**, 475. DOI. ADS.
- Soler, R., Goossens, M., Terradas, J., Oliver, R.: 2013, The behavior of transverse waves in nonuniform solar flux tubes. I. Comparison of ideal and resistive results. *Astrophys. J.* **777**, 158. DOI. ADS.
- Soler, R., Goossens, M., Terradas, J., Oliver, R.: 2014, The behavior of transverse waves in nonuniform solar flux tubes. II. Implications for coronal loop seismology. *Astrophys. J.* **781**, 111. DOI. ADS.
- Spruit, H.C.: 1982, Propagation speeds and acoustic damping of waves in magnetic flux tubes. *Solar Phys.* **75**, 3. DOI. ADS.
- Terradas, J., Andries, J., Goossens, M.: 2007, On the excitation of leaky modes in cylindrical loops. *Solar Phys.* **246**, 231. DOI. ADS.
- Terradas, J., Oliver, R., Ballester, J.L.: 2006, Damped coronal loop oscillations: time-dependent results. *Astrophys. J.* **642**, 533. DOI. ADS.
- Tomczyk, S., McIntosh, S.W.: 2009, Time-distance seismology of the solar corona with CoMP. *Astrophys. J.* **697**, 1384. DOI. ADS.
- Uchida, Y.: 1970, Diagnosis of coronal magnetic structure by flare-associated hydromagnetic disturbances. *Publ. Astron. Soc. Japan* **22**, 341. ADS.
- Vasheghani Farahani, S., Hornsey, C., Van Doorselaere, T., Goossens, M.: 2014, Frequency and damping rate of fast sausage waves. *Astrophys. J.* **781**, 92. DOI. ADS.
- Zajtsev, V.V., Stepanov, A.V.: 1975, On the origin of pulsations of type IV solar radio emission. Plasma cylinder oscillations (I). *Issled. Geomagn. Aëron. Fiz. Solnca* **37**, 3. ADS.
- Zaqarashvili, T.V., Erdélyi, R.: 2009, Oscillations and waves in solar spicules. *Space Sci. Rev.* **149**, 355. DOI. ADS.